Pressure-induced evolution of superconductivity and structural stability in a bulk $4H_b$ -TaSeS heterostructure

Yehua Huang,[1,*] Hang Li,[1,*] Xin Yang,[1,†] Wenju Zhou,[1] Donghan Jia,[1] Jiajia Feng,[1] He Zhang,[2] Guoliang Niu,[1] Bingmin Yan,[1] Fuyang Liu,[1] Qingchao Zeng,[1] Guangwei Che,[1] Runze Jiang,[1] Junwei Li,[3] Luhong Wang,[4] Haozhe Liu,[1] Ricardo D. dos Reis,[5] Renbiao Tao,[1] Xiaohui Yu,[2] Qingyang Hu,[1] Bin Chen,[1] and Huiyang Gou[1,‡]

[1]*Center for High Pressure Science and Technology Advanced Research (HPSTAR), Beijing 100193, China*

[2]*Beijing National Laboratory for Condensed Matter Physics and Institute of Physics, Chinese Academy of Sciences, Beijing 100190, China*

[3]*State Key Laboratory of Deep Earth Processes and Resources, Guangzhou Institute of Geochemistry, Chinese Academy of Sciences, Guangzhou 510640, China*

[4]*Shanghai Key Laboratory of Material Frontiers Research in Extreme Environments, Shanghai Advanced Research in Physical Sciences, Shanghai 201203, China*

[5]*Brazilian Synchrotron Light Laboratory (LNLS), Brazilian Center for Research in Energy and Materials (CNPEM), 13083-970 Campinas, SP, Brazil*

(Received 6 January 2025; revised 13 March 2025; accepted 18 March 2025; published 8 April 2025)

Transition-metal dichalcogenides (TMDs) are characterized by their unique layered structures and diverse electronic properties. Recent studies have highlighted the distinctive superconducting and charge density wave (CDW) behaviors of $4H_b$-TaS_2 and $4H_b$-$TaSe_2$. To explore the intriguing characteristics of these structurally modulated compounds, we synthesized $4H_b$-TaSeS, which alternates between $1H$ and $1T$ layers, and investigated its structural and superconducting properties. At ambient pressure, $4H_b$-TaSeS displays superconductivity with a transition temperature (T_c) of approximately 3.8 K. Under increasing pressure, T_c decreases to a minimum of around 2.3 K at 37 GPa, followed by a gradual recovery that forms an unusual valley in the T_c-pressure curve. High-pressure synchrotron x-ray diffraction measurements show that $4H_b$-TaSeS maintains its hexagonal symmetry up to 82 GPa without undergoing any structural transitions. Resistivity measurements also indicate a transition from non-Fermi liquid to Fermi liquid behavior induced by pressure. Further theoretical calculations shed light on the pressure-dependent superconducting mechanism, demonstrating that superconductivity is primarily influenced by Ta atoms, with contributions predominantly from H-layer Ta at lower pressures, gradually shifting to T-layer Ta as pressure increases. These findings offer valuable insights into pressure-induced superconductivity in TMDs and other complex layered systems.

DOI: 10.1103/PhysRevB.111.144103

I. INTRODUCTION

Transition-metal dichalcogenides (TMDs) have garnered significant interest because of their unique structural configurations and a range of physical properties, including superconductivity, charge density waves (CDW), and topological characteristics [1–4]. TMDs, represented by the general formula MX_2 (where $X = \mathrm{S}, \mathrm{Se}, \mathrm{Te}$), are layered materials characterized by a central transition metal atom (M) coordinated by six neighboring chalcogen atoms (X) in a $X - M - X$ arrangement. This configuration results in either trigonal prismatic (H-layer) or octahedral (T-layer) structures, leading to diverse crystalline phases such as $1T$, $2H$, $3R$, $4H_a$, and $4H_b$ [4–9]. These materials exhibit complex phase diagrams featuring numerous structural phase transitions, particularly under external conditions such as high pressure. As one of the most studied TMDs, tantalum disulfide (TaS_2) hosts a rich variety of crystal structures and electronic properties. For instance, $1T$-TaS_2 exhibits three successive CDW states at different temperatures and transitions to a superconducting state under high pressure [10,11]. In contrast, $2H$-TaS_2 demonstrates metallic behavior, with the coexistence of a commensurate CDW at 78 K and superconductivity at 0.8 K [12,13]. Notably, the heterojunction material $4H_b$-TaS_2, comprising alternating $1H$-TaS_2 (metallic) [14] and $1T$-TaS_2 (Mott-insulating) [15] layers stacked along the c axis. The unique arrangement leads this quasi-two-dimensional (Q2D) heterostructure to enhanced superconductivity with $T_c \sim$ 2.7–3.7 K, nearly threefold higher than that of bulk $2H$-TaS_2 [16,17]. The coexistence of metallic and insulating phases, coupled with interlayer interactions, provides an excellent platform for exploring the competition and synergy between CDW and superconductivity [13,17–22].

With regard to the tuning of the electron system, isovalent substitution has emerged as an effective approach for modulating TMD properties without introducing additional electrons or holes. Substituting sulfur (S) with selenium (Se) in $4H_b$-TaS_2 profoundly modifies its structural and electronic properties [23–25]. The incorporation of Se into the

*These authors contributed equally to this work.
†Contact author: xin.yang2@hpstar.ac.cn
‡Contact author: huiyang.gou@hpstar.ac.cn

lattice increases the interlayer distance, reduces interlayer charge transfer, and alters CDW order. These changes affect electron-correlation-driven phenomena such as superconductivity and Mott insulating behavior [26–28]. Notably, in the $4H_b$-$TaSe_xS_{2-x}$ system, the superconducting transition temperature increases to ~ 4.1 K at optimal compositions, illustrating the impact of chemical substitution [29,30]. The superconductivity and CDW phase are found to be coexistent in a wide doping range [29,30]. The H layer primarily contributes to superconductivity, whereas the T layer predominantly exhibits Mott insulating behavior, as evidenced by $TaS_{1.3}Se_{0.7}$. Additionally, Se substitution affects the interplay between the H and T layers, reducing interlayer hybridization and charge transfer.

As another powerful tool, high pressure also offers a clean method for modulating structural and electronic properties of TMDs. For $4H_b$-TaS_2, high-pressure studies reveal the emergence of a third CDW at 2.0 GPa, which disappears above 11.5 GPa, concomitant with enhanced superconductivity. Similarly, in $4H_b$-$TaSe_2$, superconductivity competes with intralayer and interlayer CDW orders, with pressure suppressing CDW and boosting superconductivity continuously [31,32]. It reveals that pressure enhances superconductivity not only within individual layers but also across neighboring layers, thereby facilitating a form of double-layer superconductivity as the CDW order collapses [33]. These findings highlight the role of pressure in unraveling the complex interplay between structural and electronic properties.

The $4H_b$-$TaSe_xS_{2-x}$ system provides an excellent platform for exploring electron-correlation-driven quantum phenomena under high-pressure conditions [29,30]. Particularly, $4H_b$-TaSeS ($4H_b$-$TaSe_xS_{2-x}$, $x = 1$) is highly attractive owing to its balanced Se and S composition, which enables precise tuning of interlayer interactions. Motivated by these insights, we synthesized $4H_b$-TaSeS using high-pressure cubic anvil press, featuring alternating T and H layers of TaSeS. Although the CDW behaviors of $4H_b$-$TaSe_xS_{2-x}$ system have been extensively studied [28,29], the superconductivity of isovalently substituted systems remains unexplored under high pressure. We systematically examined the crystal structure and electronic properties of $4H_b$-TaSeS under both ambient and high-pressure conditions, aiming to elucidate the interplay between superconductivity and structural transitions influenced by sulfur and selenium. Our results demonstrate a distinctive pressure-dependent behavior, with T_c exhibiting a valley-shaped trend, reaching a minimum near 37 GPa. Structural analysis confirmed a transition from quasi-2D to quasi-3D stacking across this pressure range, corresponding to the observed superconducting trends. This study enhances the understanding of the intricate relationship between structural and electronic properties in TMDs and contributes to further understanding of electronic structure modifications induced by the substitution of homologous elements and structural changes in similar TMDs materials under high pressure.

II. EXPERIMENTAL AND COMPUTATIONAL DETAILS

$4H_b$-TaSeS was synthesized by high-pressure cubic anvil press. High-purity starting materials of Ta, Se, and S were pressed into pellets of approximately 3.5 mm in diameter and 3 mm in thickness with an equal ratio of Ta:Se:S and were loaded in a cylindrical hexagonal BN crucible. The crucible was surrounded by a graphite sleeve resistance heater and inserted into a pyrophyllite cube as a pressure transmitting medium. The pyrophyllite cell was then placed inside a high-pressure cubic anvil press and cold pressed to 5 GPa. Then, the cell was fast brought to 1400 °C at 1200 °C/h, held for 30 min at this temperature and then slowly cooled to 800 °C before being quenched to room temperature. The chemical composition and microscopic morphology of $4H_b$-TaSeS were checked by energy dispersive spectroscopy (EDS) and scanning electron microscope (SEM). The single crystals, with sizes tens to hundred of microns, were selected from the synthesized samples and checked by single-crystal x-ray diffraction (SXRD) using Bruker D8 Venture SXRD with multilayer monochromator Mo K_α radiation ($\lambda = 0.71073$ Å). Structures were solved by dual space methods (SHELXT) [34] and refined by full-matrix least-squares on F^2 (SHELXL) using the graphical user interface ShelXle [35]. Electronic transport properties were measured by a physical property measurement system and magnetic properties were measured by a magnetic property measurement system. High pressure was created by nonmagnetic Diamond-anvil cell with anvil culets of 200 μm in diameter, and the Be-Cu gasket was covered by a cubic BN insulator layer with a diameter of ~80 μm, which was drilled as the sample chamber. The pressure-transmitting medium was KBr. *In situ* high-pressure powder x-ray diffraction (PXRD) experiments were carried out at Extreme Methods of Analysis beamline (EMAO) of the Brazilian Light Source, SIRIUS ($\lambda = 0.4859$ Å) [36] using Mao-Bell type diamond anvil cell with 200 μm culet anvils and Rhenium gaskets. The pressure dependence of ruby fluorescence was used to calibrate the pressure in the lower range [37] while the Raman spectrum of diamond was employed as a pressure calibrant in the higher region [38]. The XRD image integrations were processed using the Dioptas program [39] and then the XRD patterns were fitted using GSASII software [40].

Because of partial occupancy of the S and Se sites in the TaSeS structure, we utilized the electrostatic energy criterion in the Python Materials Genomics (pymatgen) code to determine the optimal arrangement of these atoms [41,42]. Structural relaxations and electronic property calculations were conducted using the Vienna *Ab initio* Simulation Package (VASP) within the density functional theory (DFT) framework [43,44]. The Perdew-Burke-Ernzerhof (PBE) functional within the generalized gradient approximation (GGA) was employed for the exchange-correlation potential [45]. The electron-ion interactions were described using the all-electron projector augmented wave (PAW) method [46], with Ta, S, and Se treated as having $5d^36s^2$, $3s^23p^4$, and $4s^24p^4$ valence states, respectively. A plane-wave energy cutoff of 500 eV and a Monkhorst-Pack k-point grid with a spacing of $2\pi \times 0.03$ Å^{-1} were used to sample the Brillouin zone, ensuring convergent enthalpy calculations within 1 meV/atom [47]. Phonon calculations for assessing the dynamic stability of predicted phases were performed using the finite displacement method in the PHONOPY code [48]. The crystal orbital Hamilton populations (COHP) were employed as implemented in the LOBSTER package [49–51]. Electron-phonon

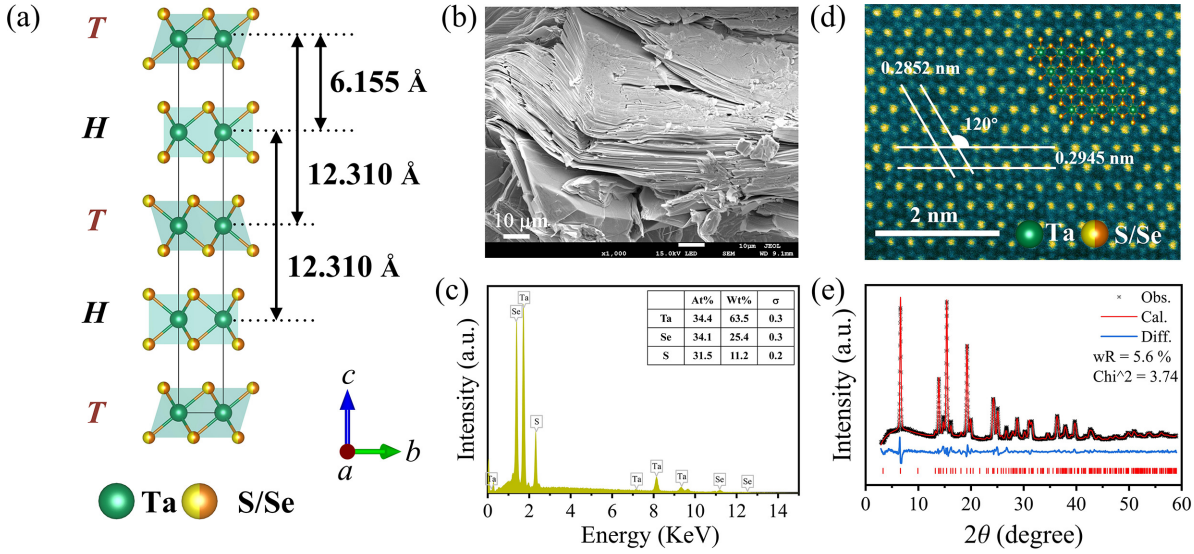

FIG. 1. (a) Crystal structure of 4H_b-TaSeS under ambient conditions. (b) The SEM image of 4H_b-TaSeS, showing the cleaved layered morphology along the c axis. (c) The EDS spectrum. (d) HAADF STEM image of 4H_b-TaSeS. (e) Rietveld refinement profiles of 4H_b-TaSeS.

coupling was analyzed within density functional perturbation theory using the QUANTUM ESPRESSO package with ultrasoft pseudopotentials [52].

III. RESULTS AND DISCUSSION

The crystal structure of 4H_b-TaSeS, synthesized under pressure, was determined by SXRD, revealing that it belongs to the space group $P6_3/mmc$ (No. 194), which is similar to 4H_b-TaS_2 and 4H_b-$TaSe_2$ but with co-occupancy of the Se and S atoms. The lattice parameters are $a = b = 3.397(7)$ Å and $c = 24.62(5)$ Å (see Tables 1– 3 within the Supplemental Material, SM [53] for structural information), consistent with previous reports [29,30]. Scanning electron microscopy (SEM) images [Fig. 1(b)] show a cleaved layered morphology along the c axis. Compared with the 4H_b-TaS_2 or 4H_b-$TaSe_2$ structure, the interlayer distance between the adjacent $T-T$ or $H-H$ layer in 4H_b-TaSeS (12.31 Å) is between the 4H_b-TaS_2 (11.86 Å) and 4H_b-$TaSe_2$ (12.6 Å) [33,54]. Energy dispersive spectroscopy (EDS) images [Fig. 1(c)] confirm the near-stoichiometric composition of TaSeS, with an atomic ratio of Ta: Se: S ≈ 34.4: 34.1: 31.5. Figure 1(d) shows high-angle annular dark field scanning transmission electron microscopy (HAADF STEM) image of 4H_b-TaSeS along the [001] direction. Furthermore, the PXRD pattern of 4H_b-TaSeS, refined using the Rietveld method with Mo K_α radiation [Fig. 1(e)], provides additional confirmation of the crystal structure in the bulk sample. These results demonstrate the high quality of the synthesized samples. Low-temperature electrical transport measurements under various pressures were conducted using the van der Pauw method. Figure 2(a) presents the resistance (R) as a function of temperature (T) at pressures up to 70 GPa, with the inset showing R/R_{10K} versus T. A zero-resistance state is observed at low temperatures under the lowest pressure, indicating a superconducting transition. To further confirm superconductivity at ambient conditions, we conducted temperature-dependent magnetization measurements under an applied magnetic field [Fig. 2(b)]. Both zero-field cooled (ZFC) and field-cooled (FC) modes exhibit a clear diamagnetic response, confirming that 4H_b-TaSeS is superconducting with a critical temperature T_c of 3.8 K, This T_c is notably higher than that of the bulk 4H_b-$TaSe_2$ (∼2.5 K) and 4H_b-TaS_2 (∼2.7 K) [17,33]. A similar enhancement in superconductivity has also been reported in related structures, such as 4H_b-$TaSe_xS_{2-x}$ [29,30]. Here, T_c is defined as the temperature at which the resistivity reaches 90% of its normal state value [Fig. 2(c)]. Notably, the zero-resistance state disappears above approximately 30 GPa. To further investigate superconductivity, the temperature dependence of resistance under varying magnetic fields was measured at various pressures, as shown in Fig. 2(d) (more results are shown in Fig. S1 within the SM [53]). With increasing magnetic field strength, the superconducting critical temperature declines until the zero-resistance state is completely replaced by normal resistance. As pressure increases, the superconducting critical temperature T_c decreases, reaching a minimum of approximately 2.3 K at around 37 GPa, after which T_c rises again, resulting in a valley-like behavior in the T_c versus pressure curve [Fig. 2(e)].

To investigate the structural evolution of 4H_b-TaSeS under pressure, *in situ* high-pressure synchrotron PXRD measurements were performed. Figure 3(a) displays synchrotron XRD patterns at room temperature up to approximately 82 GPa. All diffraction peaks shift to higher angles with a decrease in intensity, indicating 4H_b-TaSeS retains its ambient crystallographic symmetry. The diffraction peaks can be well indexed to a hexagonal structure with space group $P6_3/mmc$ (see Fig. S2 within the SM [53]), confirming that 4H_b-TaSeS retains its original structure at atmospheric pressure and ruling out structural phase transitions as the cause of the observed changes in superconductivity. We then extracted the structural parameters, including lattice parameters, bond lengths, and unit-cell volume, through a structural refinement analysis of the XRD patterns from ambient pressure to 82 GPa. As shown in Fig. 3(b), the lattice parameter ratios a/a_0 exhibit near-continuous compression, while c/c_0 demonstrates a clear

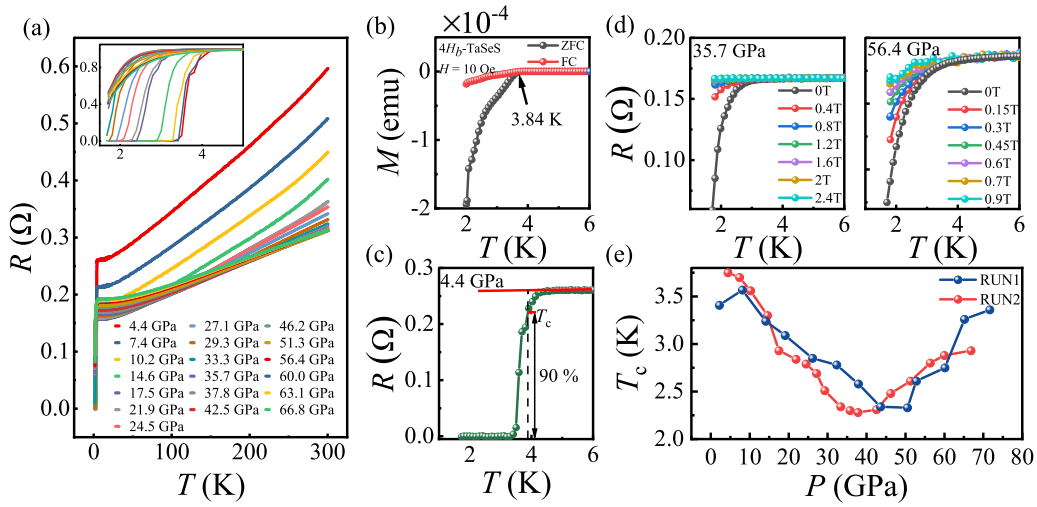

FIG. 2. (a) Temperature-dependent resistance of $4H_b$-TaSeS under various pressures. (Inset) The value of ratio $R(T)/R(10\,\mathrm{K})$ under various pressures. (b) Magnetization rate of $4H_b$-TaSeS in field-cooled and zero-field-cooled modes in the temperature range 2–6 K at a magnetic field of 10 Oe. (c) An example to illustrate the criteria used to determine the T_c, which is taken as the 90% of resistivity upon the transition. (d) Temperature dependence of resistance $R(T)$ at different magnetic fields and pressures. (e) Pressure dependence of superconducting transition temperature of $4H_b$-TaSeS.

two-stage compression behavior: rapid shrinkage for 0 GPa $\leqslant P \leqslant$ 30 GPa, followed by a linear compression rate for 30 GPa $\leqslant P \leqslant$ 82 GPa. The ratio of c/a also exhibits similar two-stage behavior. Such discontinuities in lattice parameters under varying pressure have been reported for other transition metal dichalcogenides (TMDs), such as $1T$-$TiTe_2$ [55] and $4H_b$-$TaSe_2$ [33]. The nearly pressure-independent c/a ratios observed in $4H_b$-TaSeS indicate a transformation from a quasi-2D to a quasi-3D structure. The experimental pressure-volume $(P-V)$ data are well fitted using the third-order Birch-Murnaghan equation of state (EOS) [56]. The obtained bulk modulus (K_0) is 42.5(17) GPa with $V_0 = 246.04$ Å^3 and K_0' = 7.3(4) in the range of 0 GPa $\leqslant P \leqslant$ 30 GPa (V_0 is determined by SXRD). For the range of 30 GPa $\leqslant P \leqslant$ 82 GPa, K_0 is 136.3(19) GPa with $V_0 = 221.67(4)$ Å^3 and K_0'= 3.0(3) [Fig. 3(c)].

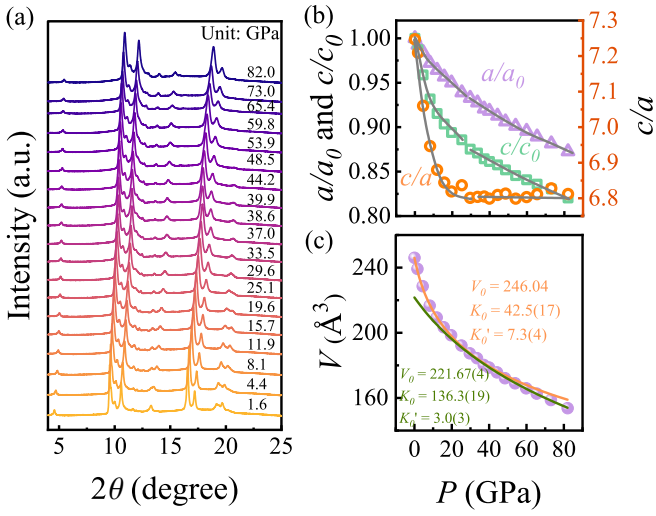

FIG. 3. (a) XRD patterns of $4H_b$-TaSeS under different pressures. (b) Pressure-dependent normalized parameters a/a_0, c/c_0, and c/a ratio extracted from the Rietveld refinements. The solid lines are guides for the eyes. (c) Pressure dependence of the volume of TaSeS fitting by the third-order Birch-Murnaghan equation of state. Solid lines are the fitting curves using the Birch-Murnaghan equation of state.

We analyzed the evolution of electrical resistance using the standard fitting model, $R(T) = R_0 + AT^n$, where R_0 is the residual resistance, A is a prefactor related to the strength of pairing interactions, and n is an exponent associated with inelastic electron scattering. In the case of electron-electron scattering, n takes on a value of 2, while in the case of electron-phonon scattering, it takes on a value of 5 [57,58]. This model effectively describes the fitted normal-state resistance $R(T)$ below 80 K. As shown in Fig. 4, the fitted exponent n increases from 1.6 to 2.2. The value of $n = 2$ is attributed to electron-electron scattering and is considered a signature of Fermi liquid (FL) behavior for the electronic spectra of the studied compound [59,60]. This demonstrates a two-stage behavior: transitioning from a non-Fermi liquid to a Fermi liquid between 0 and 30 GPa (region I), and then reverting to a non-Fermi liquid state from 30 to 70 GPa (region II). The transition from a non-Fermi liquid to a Fermi liquid is accompanied by a weakening of electron-electron interactions, which may contribute to the reduction of T_c. Conversely, the transition from a Fermi liquid back to a non-Fermi liquid enhances electron-electron interactions, potentially leading to an increase in T_c. The pressure-dependent crossover between Fermi-liquid and non-Fermi-liquid regimes plays a crucial role in governing the evolution of T_c. The initial suppression of T_c corresponds to weakened electron-electron interactions in the Fermi-liquid state, while the subsequent recovery of T_c above 30 GPa arises from strengthened correlations in the non-Fermi-liquid regime. The pre-factor A exhibits rapid shrinkage for 0 GPa $\leqslant P \leqslant$ 30 GPa, followed by near invariance for 30 GPa $\leqslant P \leqslant$ 70 GPa. Empirically, the reduction in A corresponds to a weakening of the pairing interaction strength,

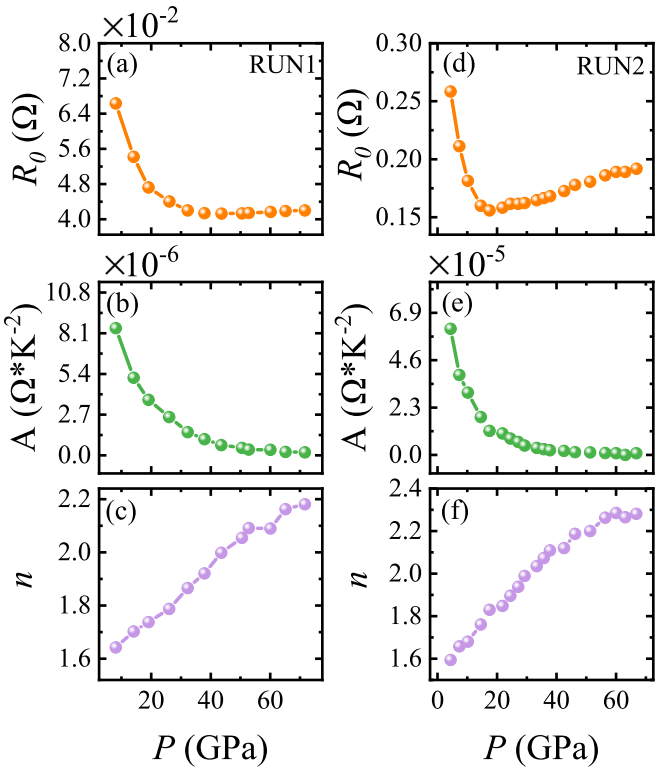

FIG. 4. The normal-state temperature dependencies of the resistance curves are fitted up to 80 K by the empirical formula $[R(T) = R_0 + AT^n]$. Pressure dependence of the residual resistance R_0, the parameter A and the exponent n (a)–(c) Run1, (d)–(f) Run2.

contributing to a decrease in T_c [57,61]. The observed gradual decrease of T_c below approximately 37 GPa aligns with this relationship.

To further explore the pressure-induced structural and superconducting behavior of TaSeS, we conducted a comprehensive search for 12- and 24-atom structures using enumeration methods, based on experimental structural data. From the resulting pool of 5 000 structures, we selected 322, including all 22 structures with 12 atoms and the 300 structures exhibiting the lowest electrostatic energy among the 24-atom configurations. We then calculated the enthalpies of these structures using density functional theory (DFT) at 0 GPa (see Fig. S3 within the SM [53]). Given that the density of states at the Fermi level (N_{EF}) is proportional to superconducting temperature according to BCS theory, we carried out electronic property calculations for the eight lowest-energy structures. As shown in Fig. S4, N_{EF} for these structures exhibits similar variations with pressure. Consequently, for our theoretical analyses, we focused on the phase with the lowest energy (see Fig. S4d within the SM [53]).

For the TaSeS structure, we conducted bonding analyses, electronic and electron-phonon coupling calculations. To estimate the structural and electronic properties at higher pressures, we extended our calculations up to 100 GPa, beyond the experimental range of 0–70 GPa. Below 20 GPa, the interlayer spacing exceeds 2 Å, and the Se-S and Se-Se bond lengths are approximately 3 Å, indicating a two-dimensional (2D) structure. Above 30 GPa, however, the Se-S and Se-Se bond lengths decrease to less than 2.8 Å, with interlayer spacings falling below 2 Å, suggesting a quasi-three-dimensional (3D) structure. This behavior aligns well with the pressure-induced transition from 2D to 3D structures observed in experimental analyses. Furthermore, the electron localization function (ELF) and crystal orbital Hamiltonian population (COHP) results reveal covalent bonding between Se-S and Se-Se in the T layer and H layer at high pressures (see Fig. S5 within the SM [53]). In contrast, the Ta-Se and Ta-S bonds exhibit ionic characteristics owing to electron transfer from Ta to Se and S atoms (see Fig. S5c within the SM [53]), with Ta atoms in the T layer transferring more electrons compared to those in the H layer.

To further understand the changes under low and high pressures, we compared the electronic band structures and density of states (DOS) of the 2D structure at 20 GPa with those of the quasi-3D structure at 60 GPa. As illustrated in Fig. S6 within the SM [53], the band structures at 20 and 60 GPa exhibit similarities. For instance, the Fermi level is predominantly contributed by T-layer Ta atoms and H-layer Ta atoms along the Y-S-X and U-R directions, respectively. In the Γ-Z-T and X-U directions, both H-layer Ta and T-layer Se atoms contribute to the Fermi level, although H-layer Ta atoms are more prominent at 20 GPa while T-layer Se atoms dominate at 60 GPa. Importantly, the contributions of N_{EF} at 20 GPa differ from those in the quasi-3D structure at 60 GPa. At 20 GPa, the contributions from Se and S atoms in both layers are similar, with H-layer Se atoms contributing slightly more. In contrast, at 60 GPa, Se atoms contribute more significantly than S atoms, and the N_{EF} for T-layer Se and S atoms slightly exceeds that of their counterparts in the H layer. Although Ta atoms remain the primary contributors to N_{EF} at both pressures, H-layer Ta atoms contribute more at 20 GPa, whereas the contributions from H-layer and T-layer Ta atoms are nearly equal at 60 GPa.

We subsequently analyzed the variation of N_{EF} from 0 to 100 GPa, as depicted in Fig. S7 within the SM [53]. Notably, N_{EF} decreases significantly below 10 GPa, exhibits a slow decline from 10 to 30 GPa, and then gradually increases from 40 to 70 GPa. This trend correlates with the experimental observations of T_c at different pressures. Throughout the pressure range of 0–100 GPa, Ta atoms consistently dominate the contributions to N_{EF}. Below 50 GPa, H-layer Ta atoms contribute more significantly than T-layer Ta atoms; however, above 50 GPa, T-layer Ta contributions surpass those from the H layer. Similar trends are observed for Se and S atoms, with their contributions transitioning from the H layer to the T layer at 40 GPa and 30 GPa, respectively. Based on these observations, we infer that superconductivity at low pressures primarily originates from the H layer, with the decline in T_c at low pressures attributed to a decrease in N_{EF} for H-layer Ta atoms. Conversely, the increase in T_c at high pressures can be attributed to the rise in N_{EF} for T-layer Ta atoms.

To analyze the superconducting mechanism of TaSeS, we conducted electron-phonon coupling simulations across pressures in the range 20–100 GPa. The phonon dispersion, phonon density of states (phDOS), Eliashberg spectral function $\alpha^2F(\omega)$, and accumulated frequency-dependent electron-phonon coupling (EPC) constants $\lambda(\omega)$ are illustrated in

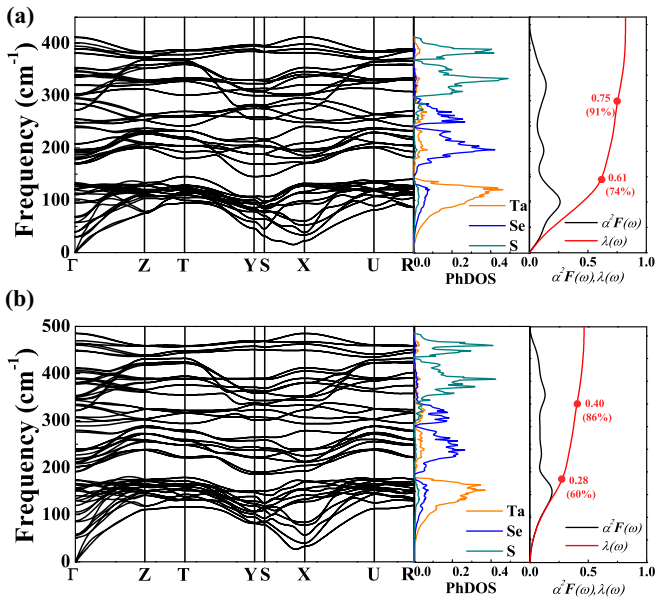

FIG. 5. Phonon dispersion relations, phonon DOS, Eliashberg spectral function, and the electron-phonon coupling parameter λ of TaSeS at (a) 20 GPa and (b) 60 GPa.

Fig. 5 and Fig. S8 within the SM [53]. At 20 GPa, the low-frequency phonon branches, primarily originating from Ta atoms, contribute approximately 74% of the total λ. Using direct numerical solutions of the Migdal-Eliashberg equations with typical Coulomb potential parameters (μ^*) of 0.1 and 0.13, the calculated T_c is around 5 K (see Fig. S9 within the SM [53]). As pressure increases, T_c decline sharply in the 20–40 GPa range, dropping to approximately 2 K. Between 50 and 70 GPa, T_c remains relatively stable, exhibiting only a negligible decline. At 80 GPa, T_c begins to slightly increase, reaching approximately 2.5 K at 100 GPa. Notably, the contribution to total λ from low-frequency phonons decreases to around 55%, still primarily derived from Ta atoms. Meanwhile, contributions from mid- and high-frequency phonons, originating mainly from Se and S atoms, gradually increase with pressure (from 17% and 9% at 20 GPa to 26% and 14% at 60 GPa, and ultimately to 27% and 18% at 100 GPa, respectively). This trend indicates that low-frequency modes predominantly contribute to superconductivity, with the decline in T_c attributed to a reduction in electron-phonon coupling strength associated with the Ta-related phonon density of states. At higher pressures, however, the enhanced contributions from mid- and high-frequency phonons, primarily from Se and S atoms, become increasingly significant for the electron-phonon coupling, which partially offsets the reduction in T_c.

IV. CONCLUSION

We synthesized a TMD heterostructure, $4H_b$-TaSeS, with a $P6_3/mmc$ space group, consisting of alternating T layers and H layers, and investigated its superconducting properties under varying pressures. At ambient pressure, superconductivity was observed in $4H_b$-TaSeS with a T_c of approximately 3.8 K. Under high-pressure conditions, we performed electrical transport measurements and synchrotron XRD to explore the evolution of its phase diagram. Our results show that T_c initially decreases from 3.8 K to a minimum of about 2.3 K at a critical pressure of approximately 37 GPa, followed by a gradual increase, forming a distinct "valley" in the T_c-pressure curve. Structural analysis suggests that near this critical pressure, $4H_b$-TaSeS undergoes a transition from a quasi-2D structure to a quasi-3D structure, which likely contributes to the observed T_c behavior. Additionally, resistivity measurements indicate a shift from non-Fermi liquid to Fermi liquid behavior, highlighting the complex nature of the electronic states in $4H_b$-TaSeS. Further theoretical calculations confirm this structural transition and show that superconductivity is primarily driven by contributions from Ta atoms. Electronic property analysis and electron-phonon coupling simulations indicate that at lower pressures, superconductivity is dominated by Ta atoms, predominantly from H-layer Ta, while at higher pressures, the main contribution to Fermi level shifts to T-layer Ta, and the contributions of Se, and S atoms to EPC gradually increase. This layer-dependent transition emphasizes the role of interlayer interactions in determining the superconducting properties of $4H_b$-TaSeS. Our findings offer insights into pressure-induced superconductivity in TMDs, providing valuable perspectives for future studies of structural and superconducting behaviors in other complex layered materials.

ACKNOWLEDGMENTS

The authors acknowledge the financial support of the National Key Research and Development Program of China (Grant No. 2023YFA1608902), the National Science Fund for Distinguished Young Scholars (Grant No. T2225027), and National Natural Science Foundation of China (Grants No. 12347157, No. 42150101). The authors acknowledge financial support from Shanghai Science and Technology Committee, China (Grant No. 22JC1410300) and Shanghai Key Laboratory Novel Extreme Condition Materials, China (Grant No. 22dz2260800). Transport properties were measured at the high-pressure synergetic measurement station of Synergetic Extreme Condition User Facility. This research used facilities of the Brazilian Synchrotron Light Laboratory (LNLS), part of the Brazilian Center for Research in Energy and Materials (CNPEM), a private non-profit organization under the supervision of the Brazilian Ministry for Science, Technology, and Innovations (MCTI). The EMA and LCTE staffs are acknowledged for the assistance during the experiments through Grants No. 20231356, No. 20231383, No. 20232992, and No. 20232956.

The authors declare no competing financial interests.

DATA AVAILABILITY

All data are available from the authors upon reasonable request.

[1] X. Qian, J. Liu, L. Fu, and J. Li, Quantum spin Hall effect in two-dimensional transition metal dichalcogenides, Science **346**, 1344 (2014).

[2] A. Splendiani, L. Sun, Y. Zhang, T. Li, J. Kim, C.Y. Chim, G. Galli, and F. Wang, Emerging photoluminescence in monolayer MoS_2, Nano Lett. **10**, 1271 (2010).

[3] M. N. Ali, J. Xiong, S. Flynn, J. Tao, Q. D. Gibson, L. M. Schoop, T. Liang, N. Haldolaarachchige, M. Hirschberger, N. P. Ong, and R. J. Cava, Large, non-saturating magnetoresistance in WTe_2, Nature (London) **514**, 205 (2014).

[4] Q. H. Wang, K. Kalantar-Zadeh, A. Kis, J. N. Coleman, and M. S. Strano, Electronics and optoelectronics of two-dimensional transition metal dichalcogenides, Nat. Nanotechnol. **7**, 699 (2012).

[5] B. Zhao, D. Shen, Z. Zhang, P. Lu, M. Hossain, J. Li, B. Li, and X. Duan, 2D metallic transition-metal dichalcogenides: Structures, synthesis, properties, and applications, Adv. Funct. Mater. **31**, 2105132 (2021).

[6] J. Wilson and A. Yoffe, The transition metal dichalcogenides discussion and interpretation of the observed optical, electrical and structural properties, Adv. Phys. **18**, 193 (1969).

[7] L. F. Mattheiss, Band structures of transition-metal-dichalcogenide layer compounds, Phys. Rev. B **8**, 3719 (1973).

[8] Q. Dong, Q. Li, S. Li, X. Shi, S. Niu, S. Liu, R. Liu, B. Liu, X. Luo, J. Si *et al.*, Structural phase transition and superconductivity hierarchy in $1T$-TaS_2 under pressure up to 100 GPa, npj Quantum Mater. **6**, 20 (2021).

[9] A. F. Kusmartseva, B. Sipos, H. Berger, L. Forró, and E. Tutiš, Pressure induced superconductivity in pristine $1T$-$TiSe_2$, Phys. Rev. Lett. **103**, 236401 (2009).

[10] B. Wang, Y. Liu, X. Luo, K. Ishigaki, K. Matsubayashi, W. Lu, Y. Sun, J. Cheng, and Y. Uwatoko, Universal phase diagram of superconductivity and charge density wave versus high hydrostatic pressure in pure and Se-doped $1T$-TaS_2, Phys. Rev. B **97**, 220504(R) (2018).

[11] K. T. Law and P. A. Lee, $1T$-TaS_2 as a quantum spin liquid, Proc. Natl. Acad. Sci. USA **114**, 6996 (2017).

[12] J. A. Wilson, F. Di Salvo, and S. Mahajan, Charge-density waves and superlattices in the metallic layered transition metal dichalcogenides, Adv. Phys. **24**, 117 (1975).

[13] D. C. Freitas, P. Rodière, M. R. Osorio, E. Navarro-Moratalla, N. M. Nemes, V. G. Tissen, L. Cario, E. Coronado, M. García-Hernández, S. Vieira, M. Núñez-Regueiro, and H. Suderow, Strong enhancement of superconductivity at high pressures within the charge-density-wave states of $2H$-TaS_2 and $2H$-$TaSe_2$, Phys. Rev. B **93**, 184512 (2016).

[14] M. H. Fischer, F. Loder, and M. Sigrist, Superconductivity and local noncentrosymmetricity in crystal lattices, Phys. Rev. B **84**, 184533 (2011).

[15] P. Fazekas and E. Tosatti, Charge carrier localization in pure and doped $1T$-TaS_2, Physica B+C **99**, 183 (1980).

[16] J. J. Gao, J. G. Si, X. Luo, J. Yan, Z. Z. Jiang, W. Wang, Y. Y. Han, P. Tong, W. H. Song, X. B. Zhu, Q. J. Li, W. J. Lu, and Y. P. Sun, Origin of the large magnetoresistance in the candidate chiral superconductor $4H_b$-TaS_2, Phys. Rev. B **102**, 075138 (2020).

[17] A. Ribak, R. M. Skiff, M. Mograbi, P. K. Rout, M. H. Fischer, J. Ruhman, K. Chashka, Y. Dagan, and A. Kanigel, Chiral superconductivity in the alternate stacking compound $4H_b$-TaS_2, Sci. Adv. **6**, eaax9480 (2020).

[18] B. Wang, Y. Liu, K. Ishigaki, K. Matsubayashi, J. Cheng, W. Lu, Y. Sun, and Y. Uwatoko, Pressure-induced bulk superconductivity in a layered transition-metal dichalcogenide $1T$-tantalum selenium, Phys. Rev. B **95**, 220501(R) (2017).

[19] R. M. Fleming and R. V. Coleman, Oscillatory magnetotransport in the layer compounds $4H_b$-TaS_2 and $2H$-$TaSe_2$, Phys. Rev. B **16**, 302 (1977).

[20] R. Fleming and R. Coleman, Oscillatory magnetoresistance in $4H_b$-TaS_2, Phys. Rev. Lett. **36**, 1555 (1976).

[21] C. G. Slough, W. W. McNairy, R. V. Coleman, B. Drake, and P. K. Hansma, Charge-density waves studied with the use of a scanning tunneling microscope, Phys. Rev. B **34**, 994 (1986).

[22] I. Sánchez-Ramírez, M. G. Vergniory, and F. de Juan, Charge transfer in heterostructures of T and H transition metal dichalcogenides, Phys. Rev. B **110**, 195138 (2024).

[23] Y. Liu, R. Ang, W. Lu, W. Song, L. Li, and Y. Sun, Superconductivity induced by se-doping in layered charge-density-wave system $1T$-$TaS_{2-x}Se_x$, Appl. Phys. Lett. **102**, 192602 (2013).

[24] S. Xu, Z. Liu, P. Yang, K. Chen, J. Sun, J. Dai, Y. Yin, F. Hong, X. Yu, M. Xue, J. Gouchi, Y. Uwatoko, B. Wang, and J. Cheng, Superconducting phase diagrams of S-doped $2H$-$TaSe_2$ under hydrostatic pressure, Phys. Rev. B **102**, 184511 (2020).

[25] L. Li, X. Deng, Z. Wang, Y. Liu, M. Abeykoon, E. Dooryhee, A. Tomic, Y. Huang, J. B. Warren, E. S. Bozin *et al.*, Superconducting order from disorder in $2H$-$TaSe_{2-x}S_x$, npj Quantum Mater. **2**, 11 (2017).

[26] D. B. McWhan, R. M. Fleming, D. E. Moncton, and F. J. DiSalvo, Reentrant lock-in transition of the charge-density wave in $2H$-$TaSe_2$ at high pressure, Phys. Rev. Lett. **45**, 269 (1980).

[27] D. B. McWhan, J. D. Axe, and R. Youngblood, Pressure dependence of the striped-to-hexagonal charge-density-wave transition in $2H$-$TaSe_2$, Phys. Rev. B **24**, 5391 (1981).

[28] Y. Geng, J. Guo, F. Meng, M. Wang, S. Mi, L. Huang, R. Xu, F. Pang, K. Liu, S. Wang, H.-J. Gao, W. Zhou, W. Ji, H. Lei, and Z. Cheng, Correlated electrons in the flat band in the charge density wave state of $4H_b$-$TaSe_xS_{2-x}$, Phys. Rev. B **110**, 115107 (2024).

[29] Y. Liu, L. Li, W. Lu, R. Ang, X. Liu, and Y. Sun, Coexistence of superconductivity and commensurate charge density wave in $4H_b$-$TaS_{2-x}Se_x$ single crystals, J. Appl. Phys. **115**, 043915 (2014).

[30] Z. Xie, M. Yang, Z. G. Cheng, T. Ying, J. G. Guo, and X. Chen, A revisit of superconductivity in $4H_b$-$TaS_{2-2x}Se_{2x}$ single crystals, J. Phys. Soc. Jpn. **92**, 054702 (2023).

[31] N. Erasmus, M. Eichberger, K. Haupt, I. Boshoff, G. Kassier, R. Birmurske, H. Berger, J. Demsar, and H. Schwoerer, Ultrafast dynamics of charge density waves in $4H_b$-$TaSe_2$ probed by femtosecond electron diffraction, Phys. Rev. Lett. **109**, 167402 (2012).

[32] S. Xu, J. Deng, J. Gao, F. Meng, L. Shi, P. Yang, N. Wang, Z. Liu, J. Sun, Y. Uwatoko, H. Lei, X. Luo, Y. Sun, N. Wang, Z. Wang, B. Wang, and J. Cheng, Emergence of strong-coupling superconductivity and quantum criticality correlated with Lifshitz transitions in the alternate stacking compound $4H_b$-TaS_2, Phys. Rev. B **109**, 144522 (2024).

[33] L. Yan, C. Ding, M. Li, R. Tang, W. Chen, B. Liu, K. Bu, T. Huang, D. Dai, X. Jin *et al.*, Modulating charge-density

wave order and superconductivity from two alternative stacked monolayers in a bulk $4H_b$-$TaSe_2$ heterostructure via pressure, Nano Lett. **23**, 2121 (2023).

[34] G. M. Sheldrick, *SHELXT*–integrated space-group and crystal-structure determination, Acta Crystallogr. A **71**, 3 (2015).

[35] C. B. Hübschle, G. M. Sheldrick, and B. Dittrich, ShelXle: a Qt graphical user interface for SHELXL, J. Appl. Crystallogr. **44**, 1281 (2011).

[36] R. D. dos Reis, U. F. Kaneko, B. A. Francisco, J. Fonseca Jr, M. A. Eleoterio, and N. M. Souza-Neto, Preliminary overview of the extreme condition beamline (EMA) at the new Brazilian synchrotron source (Sirius), J. Phys. Conf. Ser. **1609**, 012015 (2020).

[37] H.-K. Mao and P. M. Bell, High-pressure physics: the 1-megabar mark on the ruby R_1 static pressure scale, Science **191**, 851 (1976).

[38] Y. Akahama and H. Kawamura, Pressure calibration of diamond anvil Raman gauge to 310 GPa, J. Appl. Phys. **100**, 043516 (2006).

[39] C. Prescher and V. B. Prakapenka, DIOPTAS: a program for reduction of two-dimensional x-ray diffraction data and data exploration, High Press. Res. **35**, 223 (2015).

[40] B. H. Toby and R. B. Von Dreele, GSAS-II: the genesis of a modern open-source all purpose crystallography software package, J. Appl. Cryst. **46**, 544 (2013).

[41] S. P. Ong, W. D. Richards, A. Jain, G. Hautier, M. Kocher, S. Cholia, D. Gunter, V. L. Chevrier, K. A. Persson, and G. Ceder, Python materials genomics (pymatgen): A robust, open-source python library for materials analysis, Comput. Mater. Sci. **68**, 314 (2013).

[42] P. P. Ewald, Die Berechnung optischer und elektrostatischer Gitterpotentiale, Ann. Phys. (Leipzig) **369**, 253 (1921).

[43] Y. Wang and J. P. Perdew, Spin scaling of the electron-gas correlation energy in the high-density limit, Phys. Rev. B **43**, 8911 (1991).

[44] G. Kresse and J. Furthmüller, Efficient iterative schemes for *ab initio* total-energy calculations using a plane-wave basis set, Phys. Rev. B **54**, 11169 (1996).

[45] J. P. Perdew and Y. Wang, Accurate and simple analytic representation of the electron-gas correlation energy, Phys. Rev. B **45**, 13244 (1992).

[46] P. E. Blöchl, Projector augmented-wave method, Phys. Rev. B **50**, 17953 (1994).

[47] H. J. Monkhorst and J. D. Pack, Special points for Brillouin-zone integrations, Phys. Rev. B **13**, 5188 (1976).

[48] A. Togo, F. Oba, and I. Tanaka, First-principles calculations of the ferroelastic transition between rutile-type and $CaCl_2$-type SiO_2 at high pressures, Phys. Rev. B **78**, 134106 (2008).

[49] R. Dronskowski and P. E. Bloechl, Crystal orbital Hamilton populations (COHP): Energy-resolved visualization of chemical bonding in solids based on density-functional calculations, J. Phys. Chem. A **97**, 8617 (1993).

[50] S. Maintz, V. L. Deringer, A. L. Tchougréeff, and R. Dronskowski, LOBSTER: A tool to extract chemical bonding from plane-wave based DFT, J. Comput. Chem. **37**, 1030 (2016).

[51] V. L. Deringer, A. L. Tchougréeff, and R. Dronskowski, Crystal orbital Hamilton population (COHP) analysis as projected from plane-wave basis sets, J. Phys. Chem. A **115**, 5461 (2011).

[52] P. Giannozzi, S. Baroni, N. Bonini, M. Calandra, R. Car, C. Cavazzoni, D. Ceresoli, G. L. Chiarotti, M. Cococcioni, I. Dabo *et al.*, QUANTUM ESPRESSO: A modular and open-source software project for quantum simulations of materials, J. Phys. Condens. **21**, 395502 (2009).

[53] See Supplemental Material at http://link.aps.org/supplemental/10.1103/PhysRevB.111.144103 for structural information, calculated energy and electronic properties of $4H_b$-TaSeS.

[54] A. Almoalem, I. Feldman, I. Mangel, M. Shlafman, Y. E. Yaish, M. H. Fischer, M. Moshe, J. Ruhman, and A. Kanigel, The observation of π-shifts in the little-parks effect in $4H_b$-TaS_2, Nat. Commun. **15**, 4623 (2024).

[55] V. Rajaji, U. Dutta, P. C. Sreeparvathy, S. C. Sarma, Y. A. Sorb, B. Joseph, S. Sahoo, S. C. Peter, V. Kanchana, and C. Narayana, Structural, vibrational, and electrical properties of $1T$-$TiTe_2$ under hydrostatic pressure: Experiments and theory, Phys. Rev. B **97**, 085107 (2018).

[56] J. Gonzalez-Platas, M. Alvaro, F. Nestola, and R. Angel, *EosFit7-GUI:* A new graphical user interface for equation of state calculations, analyses and teaching, J. Appl. Crystallogr. **49**, 1377 (2016).

[57] M. Nunez-Regueiro, G. Garbarino, and M. D. Núñez-Regueiro, The relationship between the normal state Fermi liquid scattering rate and the superconducting state, J. Phys.: Conf. Ser. **400**, 022085 (2012).

[58] D. Forsythe, S. R. Julian, C. Bergemann, E. Pugh, M. J. Steiner, P. L. Alireza, G. J. McMullan, F. Nakamura, R. K. W. Haselwimmer, I. R. Walker, S. S. Saxena, G. G. Lonzarich, A. P. Mackenzie, Z. Q. Mao, and Y. Maeno, Evolution of fermi-liquid interactions in Sr_2RuO_4 under pressure, Phys. Rev. Lett. **89**, 166402 (2002).

[59] H. v. Löhneysen, A. Rosch, M. Vojta, and P. Wölfle, Fermi-liquid instabilities at magnetic quantum phase transitions, Rev. Mod. Phys. **79**, 1015 (2007).

[60] W. Lawrence and J. Wilkins, Umklapp electron-phonon scattering in the low-temperature resistivity of polyvalent metals, Phys. Rev. B **6**, 4466 (1972).

[61] X. M. Zhao, K. Zhang, Z. Y. Cao, Z. W. Zhao, V. V. Struzhkin, A. F. Goncharov, H. K. Wang, A. G. Gavriliuk, H. K. Mao, and X. J. Chen, Pressure tuning of the charge density wave and superconductivity in $2H$-TaS_2, Phys. Rev. B **101**, 134506 (2020).